ACS OMEGA

Open Access

http://pubs.acs.org/journal/acsodf

Article

Dual-Modal Aptasensor for Sensitive Detection of Non-Small Cell Lung Cancer Exosomes Utilizing Two-Dimensional Nanopaper Co@g-C_3N_4@PB

Xin Xu, Ze Zhang, Hongwei Yu, Tong Shen, Hongzhi Pan,* and Dong Chang*

Cite This: *ACS Omega* 2024, 9, 34493−34506

Read Online

ACCESS | Metrics & More | Article Recommendations | Supporting Information

ABSTRACT: Nonsmall cell lung cancer (NSCLC), due to its lack of early symptoms, has become one of the leading causes of cancer-related deaths globally. Exosomes, small membrane vesicles secreted by cells, are widely present in human bodily fluids. In the bodily fluids of NSCLC patients, the quantity of extracellular vesicles is double that of healthy individuals, suggesting their potential as biomarkers for screening NSCLC. This study designed a dual-modal aptasensor that integrated excellent sensitivity in electrochemical detection and portability in fluorescence detection into one device. AuNPs were functionalized with exosome-capturing probes containing thiol-modified CD63 aptamers, which were immobilized on screen-printed gold electrodes. On the other hand, the carboxylated CD63 aptamer was immobilized on the surface of PB-modified g-C_3N_4 loaded with Co-SANs particles (Co@g-C_3N_4@PB). By combining these components, a sandwich structure (AuNPs/Apt1/Exo/Apt2- Co@g-C_3N_4@PB) was constructed, forming a probe for specific exosome recognition. First, the samples were preliminarily assessed for their positive or negative status under a fluorescence inverted microscope. Subsequently, a more in-depth quantitative analysis was conducted on suspected positive samples using electrochemical or fluorescence analysis methods. The detection limits for electrochemical analysis and fluorescence analysis were 66.68 and 33.5particles/mL, respectively. In the analysis of clinical serum exosome samples, the developed dual-modal aptasensor effectively distinguished serum specimens from those of NSCLC patients and healthy volunteers. This highlighted the inspection capability of the dual-modal adapter sensor, especially in point-of-care testing, making it a highly suitable tool for clinical applications.

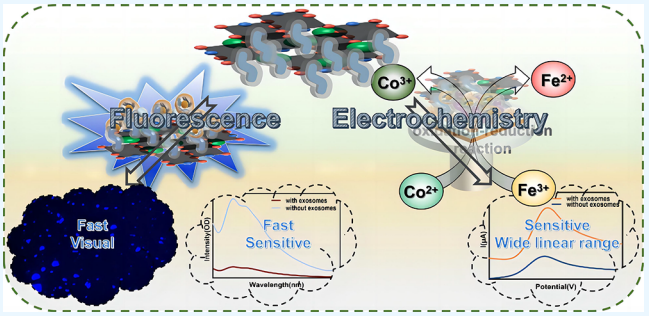

1. INTRODUCTION

The primary reason for the high mortality rate of nonsmall cell lung cancer (NSCLC) has been the fact that patients have typically progressed to advanced stages by the time of diagnosis.[1] Therefore, early screening and diagnosis of lung cancer have been deemed essential.[2] Screening for NSCLC primarily relies on low-dose computed tomography scans; however, frequent screenings can lead to cumulative radiation exposure.[3] Tissue biopsy serves as the gold standard for diagnosing NSCLC, yet the tissue heterogeneity of NSCLC determines that even with comprehensive biopsies, only a limited portion of the NSCLC tumor is represented,[4] tissue biopsy collection also poses certain limitations and risks. Tumor biomarkers are specific individual substances released during cancer cell proliferation, indicating the presence of tumors and reflecting their unique biological characteristics.[5] Compared to LDCT and tissue biopsy, tumor biomarker detection has become an extremely attractive method due to its noninvasiveness, ease of access, and excellent repeatability.[6]

Currently, tumor biomarkers primarily used for the diagnosis of NSCLC include carcinoembryonic antigen,[7] squamous cell carcinoma antigen,[8] and carbohydrate antigen 125,[9] among others. However, currently, there is no single tumor biomarker with high specificity that is reliably used for the diagnosis of NSCLC. Liquid biopsy is a noninvasive cancer diagnostic technique that involves the extraction and analysis of circulating tumor cells, circulating tumor DNA, and exosomes from patient bodily fluids. It offers advantages such as safety, noninvasiveness, repeatability, and high patient compliance.[10,11] Exosomes are small membrane-bound vesicles secreted by both normal and tumor cells, playing a crucial role in the progression of NSCLC. They can serve as diagnostic, prognostic, or predictive biomarkers for NSCLC,[12] compared to circulating tumor cells, the content of exosomes in blood is 10^9 times higher; and compared to circulating tumor DNA, exosomes originate from

Received: March 10, 2024
Revised: April 27, 2024
Accepted: May 23, 2024
Published: August 2, 2024

Scheme 1. (A) Preparation of Co@g-C_3N_4@PB, (B) Preparation of Glycine-Co@g-C_3N_4@PB-Apt2, (C) Construction of the Dual-Mode Aptasensor, and (D) Construction of the Dual-Mode Aptasensor

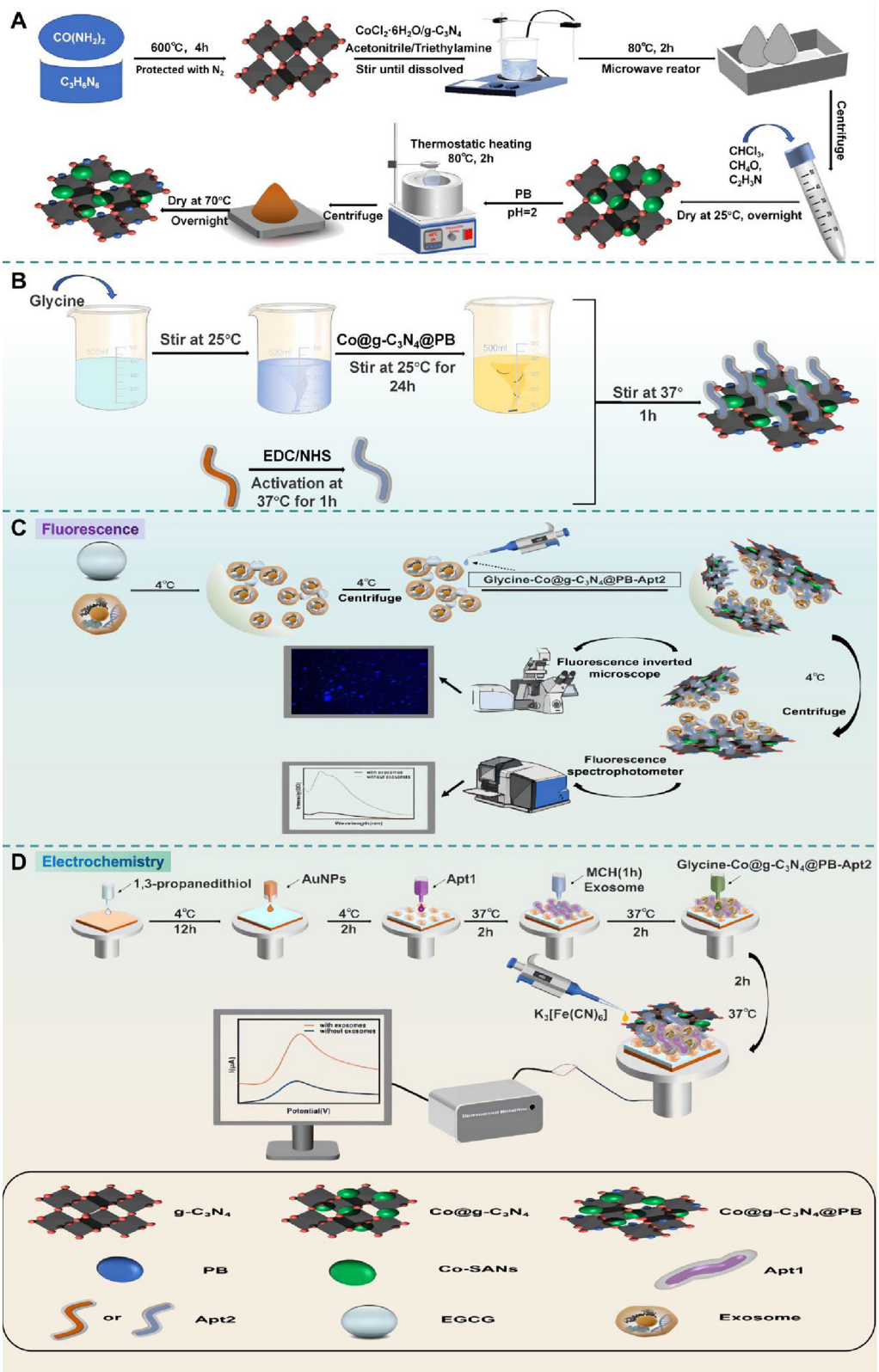

live cells, making them more representative as tumor biomarkers than circulating tumor DNA.[13,14] Additionally, studies have reported that levels of exosomes in the bodily fluids of NSCLC patients are significantly elevated compared to those of healthy individuals.[15] Therefore, exosomes are more suitable for screening NSCLC as tumor biomarkers.

The burgeoning research on exosomes is owed much to the rapid development of detection and analysis techniques for

https://doi.org/10.1021/acsomega.4c02346
ACS Omega 2024, 9, 34493−34506

exosomes. Common methods for exosome detection include nanoparticle tracking analysis (NTA),[16] transmission electron microscopy (TEM),[17] dynamic light scattering,[18] and flow cytometry.[19] However, these methods are characterized by lengthy sample processing times, intricate procedures, high costs, and low efficiency, thereby limiting their clinical utility. The aptasensor technology, utilizing aptamer-based sensors, represents a typical biosensor approach that has rapidly developed due to its advantages such as fast response times and ease of miniaturization.[20,21]

Nucleic acid aptamers refer to a class of single-stranded DNA or RNA oligonucleotide sequences that can be rapidly synthesized in vitro and possess specific binding capabilities to target molecules.[22] The previous research reported the detection of an aptasensor for exosome electrochemical or fluorescence analysis methods. Sun et al. developed a dual-signal intrinsic self-calibrating aptasensor for precise capture of proteins and detection of specific cancer-derived exosomes by assembling black phosphorus nanosheets and MOF-formed functional hybrid films.[23] Singh et al. employed synchronous immunomagnetic enrichment for one-step quantification and combined it with enzyme-mediated signal amplification. They designed a method based on rapid cocapture for targeted enrichment and detection of exosomes derived from lung cancer in human plasma.[24]

For these aptasensors used in exosome detection included electrochemical and fluorescence methods. Most aptasensor devices typically employ a single signal output. However, electrochemical aptasensors require complex and repetitive electrode incubations, leading to significantly lengthy processing times before detecting exosomes.[25] Additionally, in fluorescence-based aptasensors, the instability of fluorescent substances often limits the detection sensitivity.[26] So far, there has been a need for novel aptamer sensor methods for effective detection of exosomes, combining the advantages of low electrochemical analysis detection limits and rapid fluorescence analysis to promote clinical diagnostics. Here, carbon and nitrogen nanosheets (g-C_3N_4)[27] are combined with cobalt-doped single-atom nanoenzymes (Co-SANs)[28] and electrochemical-label prussian blue nanoparticles (PB)[29] followed by binding with single-stranded DNA aptamers and gold nanoparticles, to form a sensing platform (Scheme 1). As a dual-modal detection platform leveraging the advantages of integrated electrochemical and fluorescence analysis methods, this platform enables efficient capture, dual-signal detection, rapid detection, and high sensitivity of NSCLC exosomes.

This study designs a dual-modal aptasensor that integrates excellent sensitivity in electrochemical detection and portability in fluorescence detection into one device. The aptasensor adopts two-dimensional nanopaper Co@g-C_3N_4@PB as a multifunctional signal probe to enhance detection capability (Scheme 1). AuNPs are functionalized with exosome-capturing probes containing thiol-modified CD63 aptamers (Apt1), which are immobilized on screen-printed gold electrodes (SPGEs). On the other hand, carboxylated CD63 aptamer (Apt2) is immobilized on the surface of PB-modified g-C_3N_4 loaded with Co-SANs particles (Co@g-C_3N_4@PB). By combining these components, a sandwich structure (AuNPs/Apt1/Exo/Apt2-Co@g-C_3N_4@PB) is constructed, forming a probe for specific exosome recognition. It is worth noting that using Co@g-C_3N_4@PB as a probe for labeling exosomes enables the aptasensor to generate dual-mode outputs, facilitating both qualitative rapid screening and sensitive quantitative measurement of exosomes simultaneously. First, the samples are preliminarily assessed for their positive or negative status under a fluorescence inverted microscope. Subsequently, more in-depth quantitative analysis is conducted on suspected positive samples using electrochemical or fluorescence analysis methods. The detection limits for electrochemical analysis and fluorescence analysis are 66.68 and 33.5particles/mL, respectively. In the analysis of clinical serum exosome samples, the developed dual-modal aptasensor effectively distinguishes serum specimens from NSCLC patients and healthy volunteers. This highlights the inspection capability of the dual-modal adapter sensor, especially in point-of-care testing, making it a highly suitable tool for clinical applications.

2. EXPERIMENTAL SECTION

2.1. Reagents and Materials. The capture sequence of Apt1 is 5′-SH-TTTTTTCACCCCACCTCGCTCCCGTGA-CACTAATGCTA-3′. The identifying aptamer sequence Apt2 is 5′-COOH-CACCCCACCTCGCTCCCGTGACAC-TAATGCTA-3′. These aptamers are obtained from Shanghai Bioengineering Technology and Service Co., Ltd. Melamine and urea are purchased from Aladdin Reagent. 1-(3-(Dimethylamino)propyl)-3-ethylcarbodiimide hydrochloride (EDC), *N*-hydroxysuccinimide sodium salt (NHS), epigallocatechin gallate (EGCG), 1,1′-dioctadecyl-3,3,3′,3′-tetramethylindolecarbocyanine perchlorate (DiI), strontium chloride hexahydrate, manganese(II) chloride tetrahydrate, anhydrous iron(III) chloride, lead chloride, zirconium(IV) chloride, and cobalt(II) chloride hexahydrate are all purchased from Macklin. Triethylamine (TEA) and acetonitrile are obtained from Beijing Chemical Factory and Beijing Tongguang Fine Chemicals. All aqueous solutions are prepared using double-distilled water (DDW).

2.2. Apparatus. All tumor cells are cultured in Galaxy 170S (Germany). TEM images are obtained using a Hitachi-7650 instrument (Tokyo, Japan). NTA characterization of exosomes is prepared using Particle Metrix110 ZetaView (Germany). Nanoflow cytometry is performed using the Flow NanoAnalyzer nanoparticle flow cytometer. Sodium dodecyl sulfate-polyacrylamide gel electrophoresis (SDS-PAGE) is conducted using a Bio-Rad electrophoresis apparatus, and images are captured with an Apalleen Omega LumG camera (USA). Nanomaterials such as Co@g-C_3N_4@PB are characterized by TEM using the FEI Talos F200X G2 instrument (USA). X-ray diffraction (XRD) experiments are conducted using the Rigaku Ultima IV instrument in Japan. All electrochemical measurements are performed using the CHI760E electrochemical workstation (Chenhua, Shanghai, China). Fluorescence spectra are recorded on a spectrophotometer (RF-5301PC, Shimadzu, Japan). Fluorescence images are obtained by a fluorescence inverted microscope (Zeiss, Germany).

2.3. Preparation of g-C_3N_4 Nanosheets. In short, 2.5 g of melamine mixes with 2.5 g of urea and heats to 600 °C under N_2 for 2 h, with a heating rate of 5 °C/min.[30]

2.4. Preparation of Co@g-C_3N_4@PB. Initially, 7.5 mL of acetonitrile is used to dissolve g-C_3N_4 and 0.012g of $CoCl_2 \cdot 6H_2O$ separately. Subsequently, 65 μL of TEA is introduced into the solution and vigorously stirred until complete dissolution. Following this, the formed precipitate is carefully separated by centrifugation and underwent sequential washing with chloroform, methanol, and acetonitrile. The resulting brown powder, denoted as Co@g-C_3N_4, is subsequently dried overnight at room temperature. After this step, 100 mg of the dried brown powder is adjusted to pH 2, 5 mg of PB is introduced, and the

https://doi.org/10.1021/acsomega.4c02346
ACS Omega 2024, 9, 34493−34506

mixture is heated to 40 °C for a duration of 3 h. The resulting precipitate is then isolated through centrifugation and subjected to overnight drying at 70 °C.

2.5. Preparation of Glycine-Co@g-C_3N_4@PB-Apt2. The Apt2 (1 μM) is activated using a solution of EDC (400 mM) and NHS (100 mM) at 37 °C for 1 h. Subsequently, 5 mg of glycine with an amino group is dissolved in 20 mL of deionized water with stirring at room temperature. Next, 10 mL of Co@g-C_3N_4@PB solution (0.075 mg/mL) is slowly added with stirring at room temperature for 24 h, glycine provides a suitable environment for the binding of Apt2 and Co@g-C_3N_4@PB. Following this, 200 μL of the glycine-Co@g-C_3N_4@PB solution is combined with the activated Apt2 mixture and allowed to react at 37 °C for an additional hour. Finally, the solution is subjected to centrifugation at 12000 rpm for 10 min to separate the precipitate. The precipitate is retained and washed with deionized water, and the resulting product, glycine-Co@g-C_3N_4@PB-aptamer solution, is obtained for subsequent experiments.

2.6. Preparation of AuNPs. We took 50 mL of a chloroauric acid solution with a concentration of 0.25 mmol/L and transfer it to three-necked flasks. We assembled the stirring, heating, and condensation reflux apparatus. Then, the mixture was stirred uniformly and the chloroauric acid solution was heated to boiling. We added 1 mL of a sodium citrate solution with a concentration of 1×10^{-2}g/mL. We continued heating to maintain the boiling of the reaction solution. We observed and recorded the changes in the color and time of the reaction solution in the flask. Once the color change of the reaction solution was completely stable, heating was stopped, stirring was continued until it cooled, and the mixture was refrigerated at 4 °C in a refrigerator.

2.7. Cell Culture and Exosome Extraction. All cells are cultured in basal medium containing 10% FBS and 1% P/S and stored in a 37 °C, 5% CO_2 incubator (F12K medium for A549 and PC3 cells, DMEM for HepG2 and HeLa cells base). When the cell density reaches 60% ∼ 70%, the SBI FBS medium is added and cultured for 48 h, and then the supernatant is collected. Cellular exosomes are extracted by ultracentrifugation and stored at −80 °C.

2.8. Exosome Characterization. Transmission electron microscopy (TEM) imaging: at room temperature, 10 μL of A549 exosome solution is drop-coated onto a copper grid and incubates for 10 min. The copper grid is rinsed with sterile distilled water, and any excess liquid is absorbed with filter paper. Subsequently, 2% uranyl acetate (10 μL) is added for negative staining for 1 min. After removing excess stain with filter paper, the grid air-dries for 2 min. TEM imaging is conducted on the copper grid. As shown in Figure S1A, most of the negatively stained exosomes appear as cup-shaped vesicles, consistent with the characteristic morphology of the exosomes. A few lipid particles with a size of 10−20 nm are also observed.

Nanoparticle tracking analysis (NTA): exosomes are diluted in PBS to a concentration of 10^7 to 10^9 particles/mL for size and mass determination. The results in Figure S1B indicate an average exosome size of 76.57 nm, demonstrating satisfactory exosome quality.

Immunoblotting: western blotting quantifies the expression differences of the CD63 protein on exosomes from A549, MCF-7, HepG2, and HeLa cells. First, the total protein content of exosomes is determined using the BCA assay. After processing samples through 10% SDS-PAGE, proteins are transferred onto nitrocellulose membranes and incubated with polyclonal antibodies overnight at 4 °C. Finally, secondary antibodies are incubated with the membrane for 1 h, and imaging is performed using a gel imaging system.

Nanoflow cytometry: exosomes are diluted to 120 μL with 30 μL of exosomes, and 30 μL of the diluted exosomes is added to 20 μL of fluorescently labeled antibodies (CD9, CD63, CD81, IgG). After thorough mixing, the mixture is incubated at 37 °C in the dark for 30 min. Then, 1 mL of precooled PBS is added, and the sample is subjected to ultracentrifugation at 4 °C and 110000*g* for 70 min. The supernatant is carefully removed, and another round of ultracentrifugation is performed. The pellet is resuspended in 50 μL of precooled 1× PBS. Samples are loaded and analyzed. According to the results in Figure S1C−F, exosome characteristic proteins CD9, CD81, and CD63 are expressed in the extracted exosomes from A549 cells.

2.9. Construction of the Electrochemical Sensing Surface. The screen-printed gold electrode (SPGE) is immersed in a 2 mM solution of 1,3-propanedithiol for 12 h to form a self-assembled monolayer of thiol. Subsequently, the gold electrode is incubated with 6 μL of AuNPs at 4 °C for 2 h. We washed the unbound AuNPs with 10 mM PBS. We dispersed the Apt1 in a 10 mM Tris-HCl buffer (including 10 mM TCEP, pH 7.4) and activated at 37 °C for 1 h to inhibit disulfide bond formation and promote Au−S bond binding. Next, 6 μL of Apt1 was added onto the surface of the AuNP-modified electrode and incubated at 37 °C for 2 h. To reduce nonspecific binding, we incubated the modified electrode with a 6 μL solution of 2 mM MCH for 1 h. The electrode iwas immersed in a 6 μL exosome suspension for 2 h to capture exosomes. Unbound exosomes are then removed by rinsing with 10 mM PBS. After that, the electrodes were incubated with glycine-Co@g-C_3N_4@PB-Apt2 solution for 2 h and washed with 0.01 M PBS buffer. The Co@g-C_3N_4@PB-Apt2/exosomes/MCH/Apt1/AuNPs/1,3-propanedithiol/SPGE was immersed in 0.5 M $Fe(CN)_6^{3-}/Fe(CN)_6^{4-}$ to form an electrochemical sensing interface and used for cyclic voltammetry (CV) measurements, with a sweep rate set to 0.1 V/s.

2.10. Fluorescence Localization Imaging and Quantitative of Exosomes. The exosome solution of different concentrations is mixed with EGCG at a concentration of 0.25 mg/mL, incubated at 4 °C, and centrifuged at 3000 rpm for 20 min, and the supernatant is removed. The precipitate and Co@g-C_3N_4@PB-Apt2 are incubated in PBS for 1 h, washed 3 times, mixed with DiI, and incubated for half an hour. They are then washed 3 times again, finally obtaining Co@g-C_3N_4@PB-Apt2 and DiI double-labeled aggregated exosomes. Fluorescence imaging is performed using a fluorescence inverted microscope. Fluorescence quantification is performed using a fluorescence spectrophotometer.

2.11. Analysis of Human Serum Exosomes. Twenty-one patients over the age of 60, diagnosed with NSCLC, and twenty-one healthy volunteers over the age of 60 are recruited from Shanghai Pudong Hospital. Serum exosomes are isolated using the exoEasy Maxi Kit (20) and stored at −80 °C. The exosomes are then detected using a dual-mode aptasensor.

3. RESULTS AND DISCUSSION

3.1. Fluorescence and Electrical Properties of Different Metal-SANs Chelation with g-C_3N_4. Since there are abundant positively charged metal ions on metal-SANs, the *z* potential value of g-C_3N_4 increases after chelation with metal-SANs. TEM characterization shows that metal-SANs are effectively loaded onto g-C_3N_4 (Figure S2B,C). As shown in

https://doi.org/10.1021/acsomega.4c02346
ACS Omega 2024, 9, 34493−34506

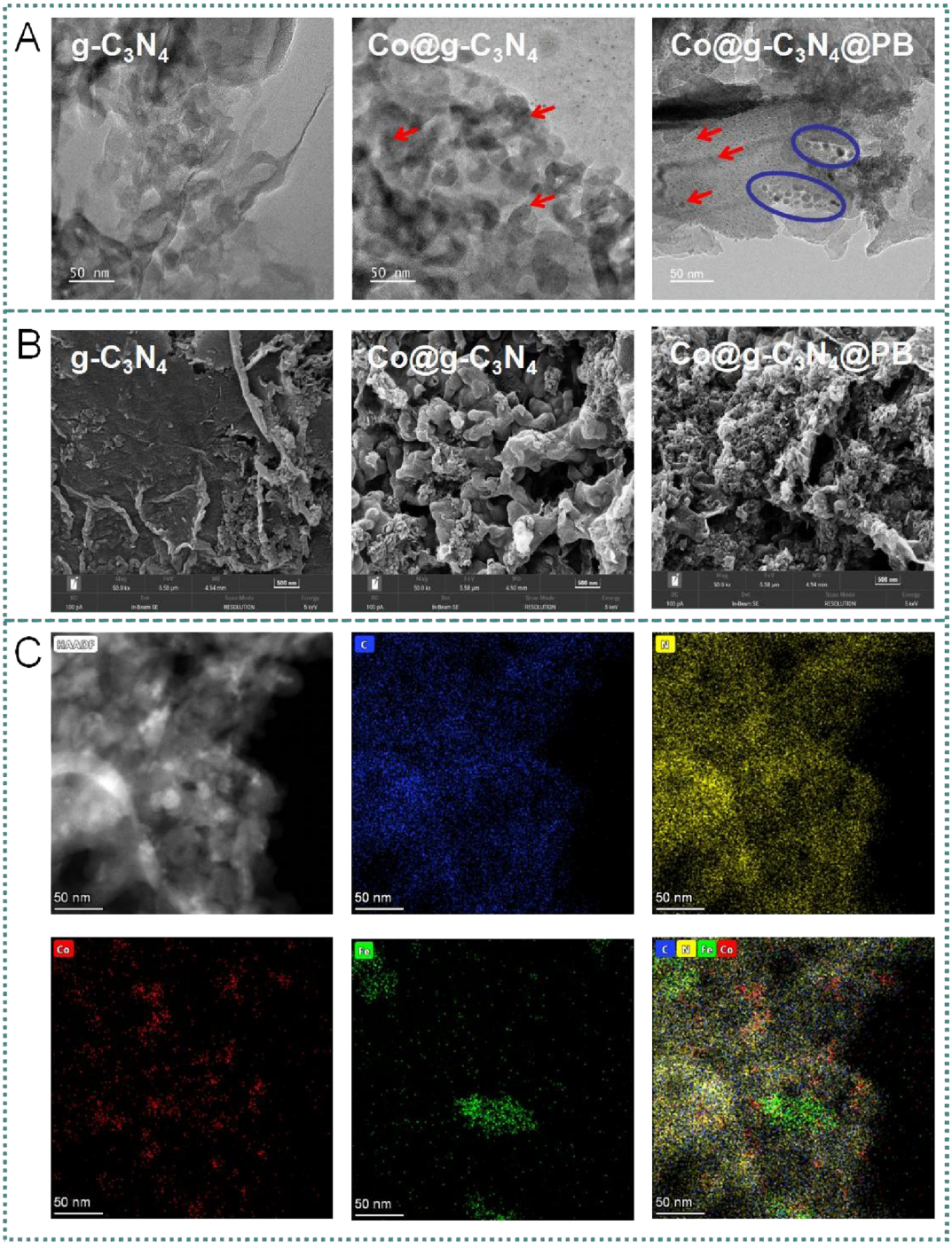

Figure 1. TEM (A) and SEM (B) characterization of g-C_3N_4,Co@g-C_3N_4, and Co@g-C_3N_4@PB. (C) Distribution of metallic elements on Co@g-C_3N_4@PB.

Figure.S2A, the *z* potentials of g-C_3N_4, Ag@g-C_3N_4, Pb@g-C_3N_4, Sr@g-C_3N_4, Te@g-C_3N_4, Zr@g-C_3N_4, and Co@g-C_3N_4 are 13.65, 27.63, 24.41, 29.90, 29.79, 26.28, and 24.31 mV, respectively. The *z* potential indicates the stability of the nanodispersion. Absolute values of *z* potentials higher than 0−10, 10−20, 20−30, and 30 mV are defined as extremely unstable, relatively stable, moderately stable, and highly stable. Therefore, compared with g-C_3N_4, Co, Te, and Ag-SANs exhibit strong stability.

Compared to organic fluorophores, g-C_3N_4 exhibits a relatively low fluorescence quantum yield due to the non-radiative nature of the lowest-energy excitons and extrinsic factors that tend to quench the nanotube fluorescence.[31] Studies indicate that the fluorescence intensity varies when different metal ions are added to the organic nanosheet solution, suggesting the potential for utilizing metal ions to enhance the g-C_3N_4 fluorescence response, facilitating optical imaging and the creation of sensing elements.[32] As illustrated in Figure S3A, resonance coupling of g-C_3N_4 emission to the reradiating dipolar plasmonic modes in the metal leads to a shortening of the radiative lifetime, resulting in enhanced fluorescence of g-C_3N_4 by Co, Pb, Te, and Zr-SANs.[33] Conversely, the

https://doi.org/10.1021/acsomega.4c02346
ACS Omega 2024, 9, 34493−34506

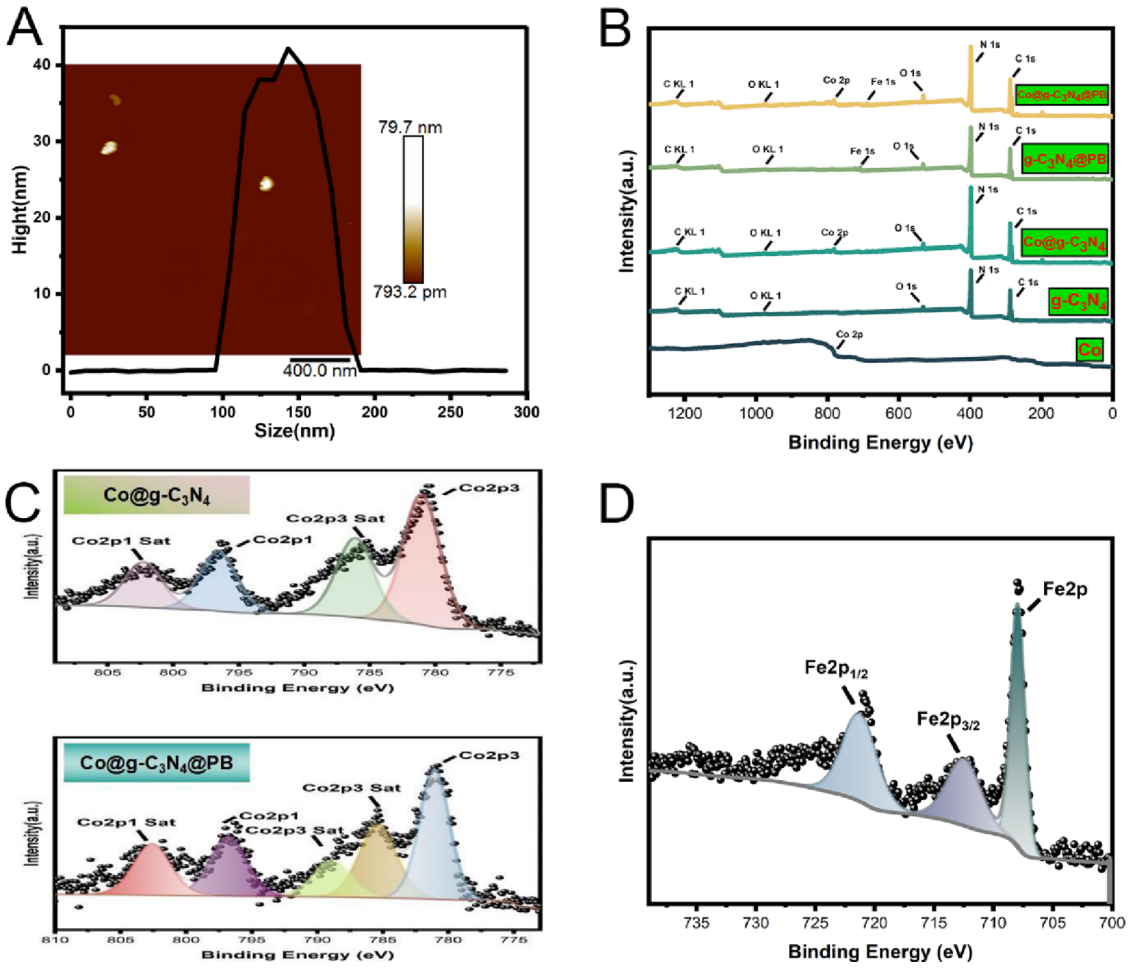

Figure 2. (A) AFM image of Co@g-C_3N_4@PB. (B) High-resolution XPS spectra of Co, g-C_3N_4, Co@g-C_3N_4, g-C_3N_4@PB, and Co@g-C_3N_4@PB. The high-resolution XPS spectra of Co 2p (C) and Fe 2p (D), respectively.

fluorescence intensity of g-C_3N_4 is quenched by Ag and Sr-SANs due to excited electron transfer from g-C_3N_4 to the metal nanoparticles.[34] A comparison with Figure S3B reveals a one-to-one correspondence between the fluorescence intensity and the fluorescence image obtained by a fluorescence inverted microscope.

Based on *z* potential and fluorescence response results, this study selects Co@g-C_3N_4, which exhibits superior photoelectric response, for the development of aptasensors. To evaluate the impact of adding PB containing Fe ions to Co@g-C_3N_4 on fluorescence, we investigate the fluorescence intensity of g-C_3N_4, Co@g-C_3N_4, Co, g-C_3N_4@PB, and Co@g-C_3N_4@PB. Co-SANs itself lack fluorescence emission properties, but loading Co-SANs and PB separately enhances the fluorescence of g-C_3N_4 due to the metal-enhanced fluorescence effect. Simultaneously loading Co-SANs and PB onto g-C_3N_4 forms Co@g-C_3N_4@PB, resulting in 1.75 times increase in fluorescence yield compared to g-C_3N_4. This illustrates the feasibility of using Co@g-C_3N_4@PB as a fluorescent probe to label exosomes for fluorescence analysis.

3.2. Material Characterization. The synthesized g-C_3N_4 is characterized by TEM scanning (Figure 1A). Co-SANs are uniformly loaded on g-C_3N_4 (red arrow in Figure 1A). After further loading of PB on Co@g-C_3N_4, PB successfully chelates with it (blue circle in Figure 1A). SEM images (Figure 1B) show that the surface of g-C_3N_4 is relatively smooth; however, with the loading of Co-SANs and PB, the surface becomes increasingly rough. Surface metal element analysis results (Figure 1C) further confirm the above findings. These results demonstrate the successful synthesis of Co@g-C_3N_4@PB.

The thickness of the Co@g-C_3N_4@PB was characterized by AFM and was approximately 38.4 nm (Figure 2A), suggesting that these are two-dimensional nanosheets with a paper-like structure. The successful synthesis of Co@g-C_3N_4@PB was confirmed by XPS patterns. the XPS spectrum changes with the loading of Co-SANs and PB on g-C_3N_4 (Figure 2B), Co@g-C_3N_4@PB shows the element peak spectrum of Co and Fe. The XPS spectrum in the Co 2p region varied from the g-C_3N_4 to Co@g-C_3N_4@PB (Figure 2C). The Co 2p spectrum of Co@g-C_3N_4 showed four peaks at 781.08 796.68, 786.96, and 802.75 eV, which can be assigned to the Co 2p3, Co 2p3 Sat, Co 2p1, and Co 2p1 Sat, respectively. However, the peak of Co 2p3 Sat in the Co@g-C_3N_4@PB changed to become 785.45 eV. In addition, a splitting peak of Co 2p3 Sat bands at 788.88 eV appeared in the Co@g-C_3N_4@PB. Meanwhile, Fe $2p_{1/2}$ and Fe $2p_{3/2}$ were observed in the Co@g-C_3N_4@PB (Figure 2D). These results provided further evidence of the successful preparation of Co@g-C_3N_4@PB.

To investigate the electrochemical behavior of Co@g-C_3N_4@PB generated in situ on the electrode surface to detect the exosomes, g-C_3N_4, Co-SANs, Co@g-C_3N_4, PB, g-C_3N_4@PB, and Co@g-C_3N_4@PB were modified on SPGE (Figure 3).

https://doi.org/10.1021/acsomega.4c02346
ACS Omega 2024, 9, 34493−34506

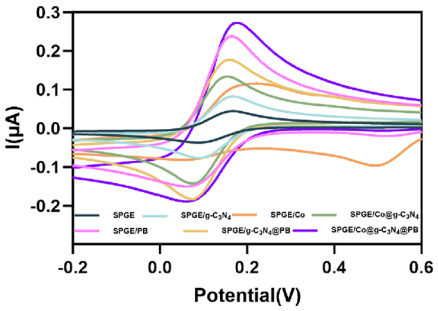

Figure 3. CV curves of the SPGE, SPGE/g-C_3N_4, SPGE/Co, SPGE/Co@g-C_3N_4, SPGE/PB, SPGE/g-C_3N_4@PB, and SPGE/Co@g-C_3N_4@PB. The electrolyte is 0.5 M $Fe(CN)_6^{3-}/Fe(CN)_6^{4-}$ in 0.5 M KCl, and the sweep rate was set to 0.1 V/s.

Obviously, due to the better conductivity of Co-SANs, when Co-SANs are under load, the peak current of g-C3N4 increases from 0.096 to 0.133 μA, and the peak voltage shifts left from 0.173 to 0.156 V. When loading PB with excellent electrocatalytic performance, compared with g-C_3N_4, the current peak value of g-C_3N_4@PB increased by 0.08 μA, and the current peak value of Co@g-C_3N_4@PB increased by 2.84 times. These results demonstrate the feasibility of constructing an aptasensor for exosome electrochemical analysis using synthesized Co@g-C_3N_4@PB.

3.3. Electrochemical Characterization of Biosensors. In a cyclic voltammetry diagram on a bare SPGE has an oxidation peak of 0.239 μA at 0.195 V(curve a), as shown in Figure 4A. After modifying the Au electrode with 1,3-propanedithiol, the self-assembled monolayer of thiol formed on the electrode surface hinders the diffusion of $Fe(CN)_6^{4-/3-}$ to the electrode surface, so the current signal is attenuated to 0.190 μA (curve b). When Apt1 binds to Au NPs, the current intensity further decreases to 0.170 μA, which is due to the negatively charged phosphate backbone of the DNA molecule restricting the diffusion of $Fe(CN)_6^{4-/3-}$ (curve c).[35] Current intensity is further reduced to 0.148 μA when MCH blocks nonspecific binding (curve d). When exosomes are enriched on the electrode surface, the current intensity decreases significantly (curve (e)) because the protein and lipid bilayers on the surface of exosomes are negatively charged. When Co@g-C_3N_4@PB-Apt2 combines with exosomes on the electrode surface, the peak current increases to 0.127 μA, which is due to the good conductivity of Co@g-C_3N_4@PB (curve f).[36] This proves that the proposed aptasensor was successfully constructed. Figure 4B displays the EIS curve. The diameter of the semicircle is equal to the electron transfer resistance (Ret) at the electrode interface. The greater the diameter, the greater the resistance and the lower the electron transfer efficiency. These results show the same trend as the CV results, demonstrating that the assembly of the aptasensor is successful.

3.4. Fluorescence Imaging of Exosomes Using the Co@g-C_3N_4@PB Probe. To monitor the capture process, exosome fluorescence imaging is performed using Co@g-C_3N_4@PB as a signal probe. First, we evaluated whether g-C_3N_4 can label exosomes. Exosomes are very small, so they need to be enriched before capture. The gallic ring on EGCG can interact with the trimethylammonium groups on the exosome membrane and form aggregate bundles based on the polyphenol−phospholipid binding mechanism[37] (Figure 5A). Therefore, EGCG can serve as an exosome preenrichment and isolation medium. Incubating with exosomes allows for easy separation using relatively small centrifugal force, thereby enabling fluorescence imaging (Figure 5B). To verify the ability of g-C_3N_4 to label exosomes, we selected the lipophilic membrane dye DiI as a reference. Exosome aggregates are simultaneously labeled with g-C_3N_4 and DiI. Weak blue (Figure 5C_{a1}) and red (Figure 5C_{a2}) fluorescence signals are observed for g-C_3N_4 and DiI, respectively. The weak purple fluorescence signal seen in Figure 5C_{a3} indicates that g-C_3N_4 and DiI are colocalized. This shows that g-C_3N_4 can enter exosome aggregates and can serve as an exosome fluorescence imaging probe that does not require ultracentrifugation. However, labeling exosomes with the g-C_3N_4 fluorescent probe produces a weak fluorescence emission. After labeling exosome aggregates with Co@g-C_3N_4@PB and DiI simultaneously, we find that due to the loading of Co-SANs and PB, the specific surface area of g-

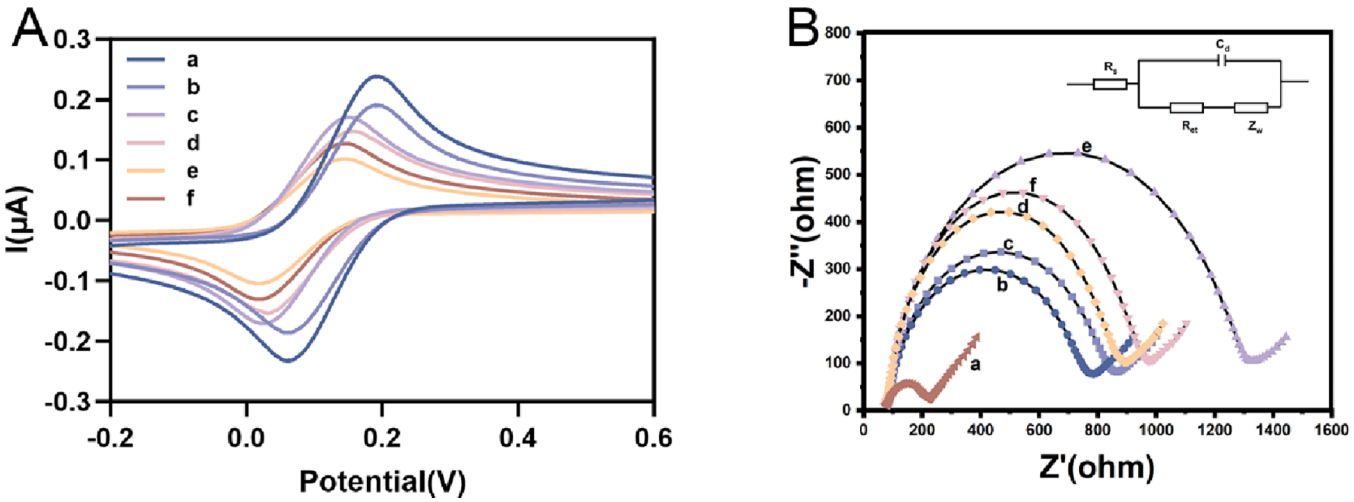

Figure 4. (A) Cyclic voltammograms and (B) electrochemical impedance spectra. (a) SPGE, (b) AuNPs/1,3-propanedithiol/SPGE, (c) Apt1/AuNPs/1,3-propanedithiol/SPGE, (d) MCH/Apt1/AuNPs/1,3-propanedithiol/SPGE, (e) exosomes/MCH/Apt1/AuNPs/1,3-propanedithiol/SPGE, and (f) Co@g-C_3N_4@PB-Apt2/exosomes/MCH/Apt1/AuNPs/1,3-propanedithiol/SPGE. The electrolyte is 0.5 M $Fe(CN)_6^{3-}/Fe(CN)_6^{4-}$ in 0.5 M KCl, the sweep rate was set to 0.1 V/s. The impedance spectra were recorded from 0.1 Hz to 100 kHz with a signal amplitude of 5 mV at the formal potential of the redox couple. The concentration of exosomes is 3×10^3 particles/mL.

https://doi.org/10.1021/acsomega.4c02346
ACS Omega 2024, 9, 34493−34506

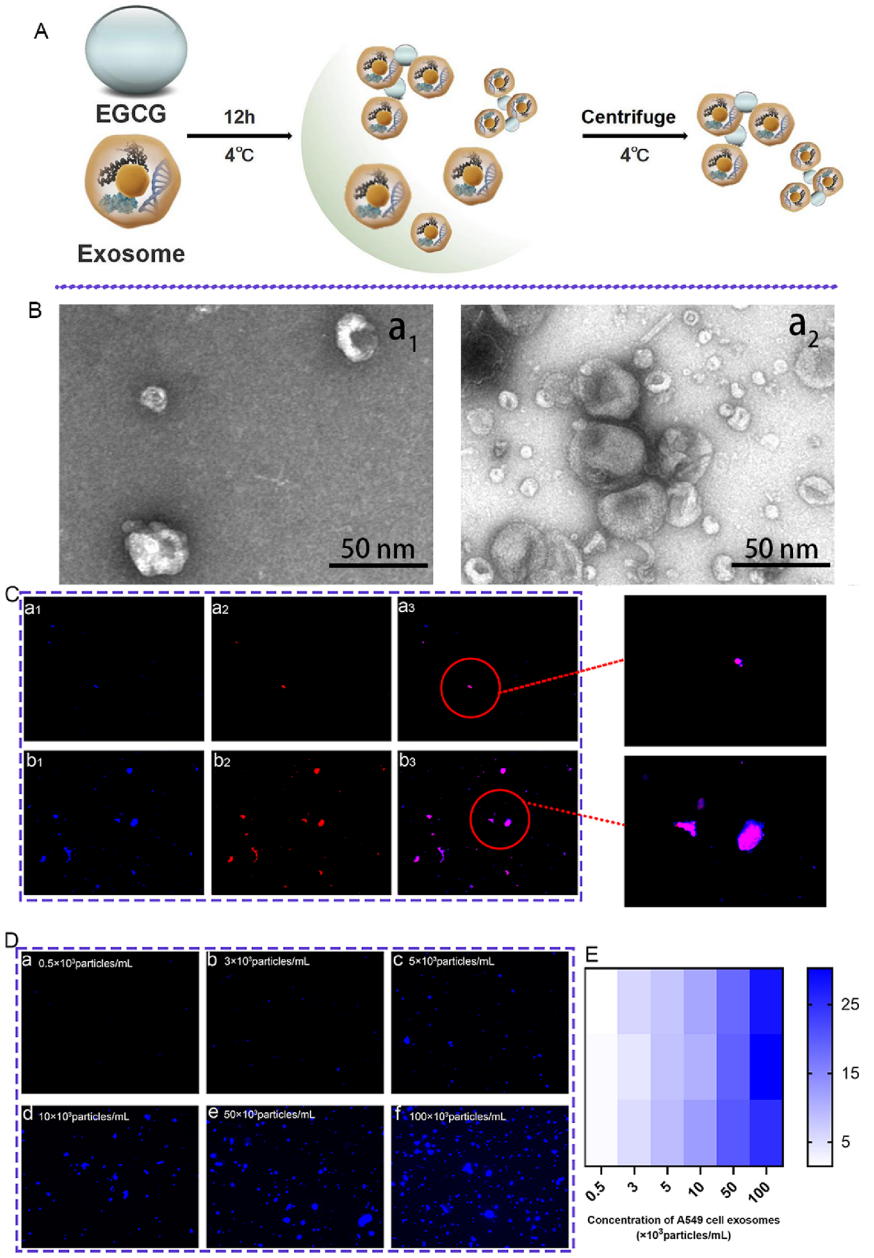

Figure 5. (A) Schematic imaging of EGCG@exosome aggregate formation. (B) TEM images of exosomes (a_1) and exosomes treated with EGCG (a_2). (C) Fluorescence imaging of exosomes aggregates stained with g-C_3N_4 (a_1), DiI (a_2), overlay of a_1 and a_2 (a_3), Co@g-C_3N_4@PB(b1), DiI (b_2), overlay of b_1 and b_2 (b_3). (D) Fluorescence imaging of exosome aggregates in A549 cells stained with Co@g-C_3N_4@PB at different concentrations (0.5×10^3–10^5particles/mL). (E) Heat map visually displays the average fluorescence intensity of fluorescence imaging of different concentrations of exosome aggregates in A549 cells stained with Co@g-C_3N_4@PB, and three parallel experiments were used to calculate the error.

C_3N_4 increases[38] and more can be enriched. The blue (Figure 5C_{b1}) and red (Figure 5C_{b2}) fluorescence signals of the exosomes are significantly enhanced. Figure 5C_{b3} shows the strong purple fluorescence emitted after the overlap of blue and red fluorescence, indicating significant colocalization between Co@g-C_3N_4@PB and DiI. Furthermore, due to the metal-enhanced fluorescence effect, utilizing Co@g-C_3N_4@PB as a labeling agent for exosomes exhibits a more pronounced fluorescence response compared to g-C_3N_4.

With the increase of exosome aggregates, Co@g-C_3N_4@PB also increases; therefore, the average fluorescence intensity increases. This change is clearly visible under a fluorescence inverted microscope (Figure 5D). After quantification of the fluorescence image through ImageJ (Figure 5E), it reflects the changes in fluorescence intensity more intuitively. These results indicate that by using Co@g-C_3N_4@PB as a fluorescence probe, exosomes can be subjected to a simple and rapid pretreatment. Initial determination of positive and negative samples can be carried out using a fluorescence inverted microscope, followed by more in-depth quantitative analysis of suspected positive samples.

3.5. Optimization of Experimental Conditions. To ensure the high performance of electrochemical and fluorescent analyses, we optimize the experimental conditions, including the concentrations of KCl and aptamers, the incubation temperature and time of exosomes, and the ratio of exosomes to Co@g-C_3N_4@PB (Figure S5). As shown in Figure S5A, to enhance the conductivity of the electrolyte solution $(Fe(CN)_6^{3-}$/Fe-

https://doi.org/10.1021/acsomega.4c02346
ACS Omega 2024, 9, 34493−34506

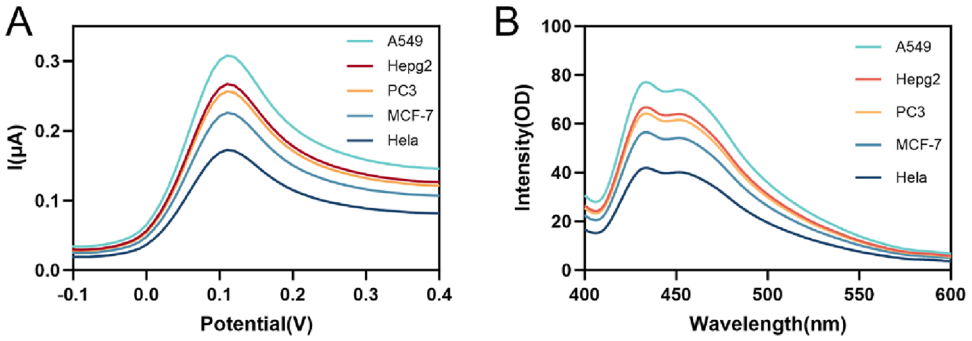

Figure 6. Electrochemical (A) and fluorescence (B) analyses detect CD63 protein on the surface of exosomes derived from A549, Hepg2, PC-3, MCF-7, and HeLa cells. The concentration of exosomes was 10^6 particles/mL. The electrolyte is 0.5 M $Fe(CN)_6^{3-}/Fe(CN)_6^{4-}$ in 0.5 M KCl, and the sweep rate was set to 0.1 V/s. The excitation wavelength is 300 nm.

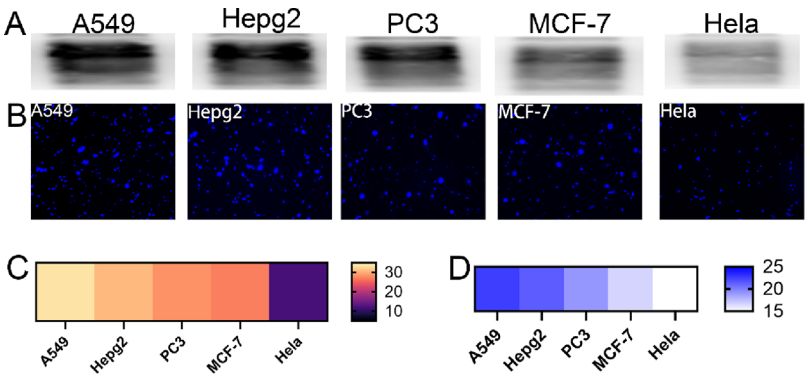

Figure 7. Western blot analysis (A) and fluorescence images (B) of CD63 protein on the surface of exosomes derived from A549, Hepg2, PC-3, MCF-7, and HeLa cells.

$(CN)_6^{4-}$), we added a certain amount of KCl solution to it. As the KCl concentration increases, the current intensity increases and then reaches a maximum value at 0.5M. Therefore, the optimal concentration of KCl is selected to be 0.5M. As shown in Figure S5B, when the concentration of Apt2 in Co@g-C_3N_4@PB increases, the current intensity gradually increases until the concentration reaches 0.8 μM. Beyond this concentration, if Apt2 exceeds Co@g-C_3N_4@PB, its ability to bind to exosomes weakens, resulting in reduced signals. Therefore, the optimal concentration of Apt2 is selected to be 0.8 μM. The temperature and duration of exosome incubation are also key considerations. As shown in Figure S5C and Figure 5F, for electrochemical and fluorescent analyses, Apt1 and Apt2 capture exosomes, respectively. However, both current intensity and fluorescence intensity reach their highest points at 37 °C, reflecting the temperature's influence on the binding efficiency of exosomes and aptamers. Additionally, with increased incubation time, fluorescence intensity rises and peaks at 120 min, attributed to exosome decomposition (Figure S5E). For fluorescence analysis, the quantity of Apt2 on Co@g-C_3N_4@PB directly impacts the sensitivity of the aptasensors. We optimized the ratio of exosomes to Co@g-C_3N_4@PB. The fluorescence intensity peaked when the volume ratio of the two was 4:5 (Figure S5D).

3.6. Protein Analysis of Cancer Cell-Derived Exosomes. To verify the capability of the constructed dual-modal aptasensor for qualitative and quantitative analysis of CD63 protein on the surface of exosomes derived from various cancer cells, we set the concentration of exosomes to 10^6 particles/mL. We detect the expression levels of CD63 protein on the surface of exosomes derived from NSCLC cells (A549), liver cancer cells (HepG2), pancreatic cancer cells (PC-3), breast cancer cells (MCF-7), and cervical cancer cells (HeLa). As shown in Figure 6, two analytical methods exhibit the same trend: CD63 protein is highly expressed in exosomes derived from A549 cells followed by HepG2 and PC-3 cells.[39,40]

At the same time, we employ conventional protein detection technology, western blotting, to further verify the expression differences of the CD63 protein on the surfaces of exosomes derived from different cancer cells. As depicted in Figure 7A, CD63 protein is expressed on the surfaces of exosomes derived from A549, HepG2, PC-3, MCF-7, and HeLa cells.[41] However, the expression level is the lowest on the surface of exosomes derived from HeLa cells.[42] The heatmap in Figure 7C intuitively illustrates significant differences in the CD63 protein on the surfaces of exosomes derived from various cancer cells. Simultaneously, we utilized a fluorescence inverted microscope to capture images of the fluorescence emitted by exosomes analyzed fluorescently (Figure 7B). The heatmap of average fluorescence intensity presented in Figure 7D visually illustrates the same trend as that in Figure 7C. The results indicate varying expression levels of CD63 protein on the surfaces of exosomes derived from diverse cancer cells, detectable through the developed dual-modal aptasensor.

The heat map visually displays the grayscale value of WB analysis results (C) and the average fluorescence intensity of fluorescence imaging (D) of the expression levels of the CD63 protein on the exosome surface of five tumor cells. The concentration of exosomes was 10^6 particles/mL.

The two analysis methods and western blot analysis results are consistent. This series of results strongly demonstrates the reliability and accuracy of the constructed dual-modal

https://doi.org/10.1021/acsomega.4c02346
ACS Omega 2024, 9, 34493−34506

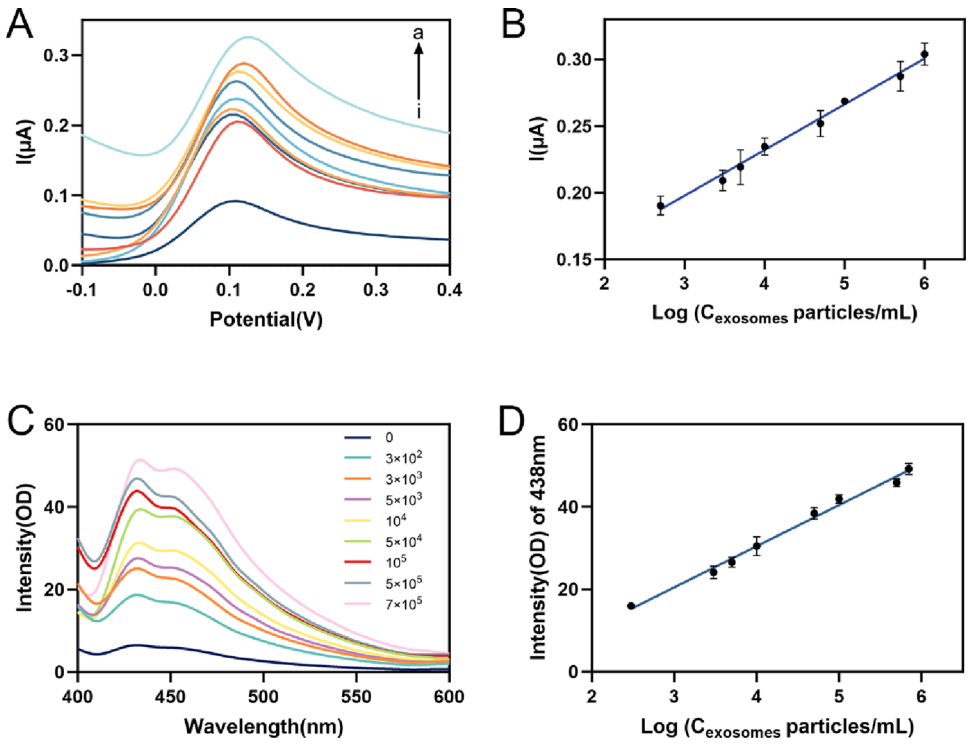

Figure 8. CV response (A) and fluorescence spectroscopy (C) curves of different exosomes concentrations (a−i: 0, 5×10^2, 3×10^3, 5×10^3, 10^4, 5×10^4, 10^5, 5×10^5, and 10^6 particles/mL). Plot of CV intensity (B) and fluorescence intensity (D) vs the logarithm value of the A549 cells derived exosomes concentration. Triplicate experiments were used to calculate error bars. The electrolyte is 0.5 M $Fe(CN)_6^{3-}/Fe(CN)_6^{4-}$ in 0.5 M KCl, and sweep rate was set to 0.1 V/s. The excitation wavelength is 300 nm.

aptasensor in selectively identifying the CD63 protein on the surface of exosomes. This is due to the specific binding between Apt1 labeled on AuNPs and Apt2 labeled on Co@g-C_3N_4@PB with the target CD63 protein. The expression level of CD63 protein on the surface of exosomes is highest in NSCLC cells. Apt1 and Apt2 accurately capture and identify the CD63 protein from NSCLC cells, aiding in the selective detection of exosomes originating from NSCLC cells. Even though the CD63 protein exhibits the highest expression levels on the surface of NSCLC-derived exosomes, it is also expressed on the surfaces of exosomes in various other diseases. Therefore, in clinical practice, it is necessary to combine the patient's clinical presentation, such as respiratory symptoms, to determine whether the patient is at high risk for NSCLC.

3.7. Exosome Detection Specificity, Reproducibility, Stability, and Specificity of the Dual-Modal Aptasensor. The performance of the aptasensor is assessed through the electrochemical analysis of varied concentrations of A549 cell-derived exosomes, conducted under optimal experimental conditions. As shown in Figure 6A, the current peak progressively rises with an increase in exosome concentration, ranging from 5×10^2 to 10^6 particles/mL. The correlation of this phenomenon can be articulated as follows:

$$I(\mu A) = 0.016 \log C_{exo} + 0.1742 \ (R^2 = 0.996)$$

where I represents the peak current observed in electrochemical analysis in the presence of exosomes and C_{exo} denotes the concentration of exosomes. The obtained correlation coefficient of 0.996 signifies a robust linear relationship between the peak current and the logarithm of the exosome concentration (Figure 6B). The limit of detection (LOD) is calculated using the formula LOD = $k \times \sigma/S$, where S represents the slope of the calibration curve, σ is the standard deviation of the blank sample, and k is the confidence parameter ($k = 3$). Applying a signal-to-noise ratio of S/N = 3, the calculated LOD is 66.68 particles/mL. With the increase of C_{exo}, I gradually strengthens. The Co@g-C_3N_4@PB labeled with Apt2 interacts specifically with exosomes through intermolecular forces, hydrogen bonds, and electrostatic interactions, forming the AuNPs/Apt1/Exo/Apt2−Co@g-C_3N_4@PB complex.[43] The gradual increase in I is attributed to the coupling of Co@g-C_3N_4@PB with the electrode surface upon the addition of exosomes, leading to redox reactions.[44] During these reactions, Co^{2+} is oxidized to Co^{3+}, while Fe^{3+} is reduced to Fe^{2+}, resulting in the generation of a strong electric current signal.[45]

Simultaneously, fluorescence analysis reveals a proportional increase in fluorescence intensity at 438 nm with the escalating concentration of exosomes (Figure 6C). Within the range of 3×10^2 to 7×10^5 particles/mL, the fluorescence intensity demonstrates a logarithmic proportionality to the C_{exo}. The equation governing the standard calibration curve is expressed as

$$\text{fluorescence intensity(OD)} = 9.982 \log C_{exo} - 9.4658 \ (R^2 = 0.991)$$

Achieving a commendable correlation coefficient of 0.991, a robust linear relationship is established between the fluorescence intensity and the logarithm of exosome concentration (Figure 6D). The formula for calculating the LOD is as follows: LOD = $k \times \sigma/S$, $k = 3$. Applying a signal-to-noise ratio of S/N = 3, the calculated LOD is 33.54 particles/mL. As the concentration of C_{exo} increases, the fluorescence intensity gradually enhances. The Co@g-C_3N_4@PB labeled with Apt2

https://doi.org/10.1021/acsomega.4c02346
ACS Omega 2024, 9, 34493−34506

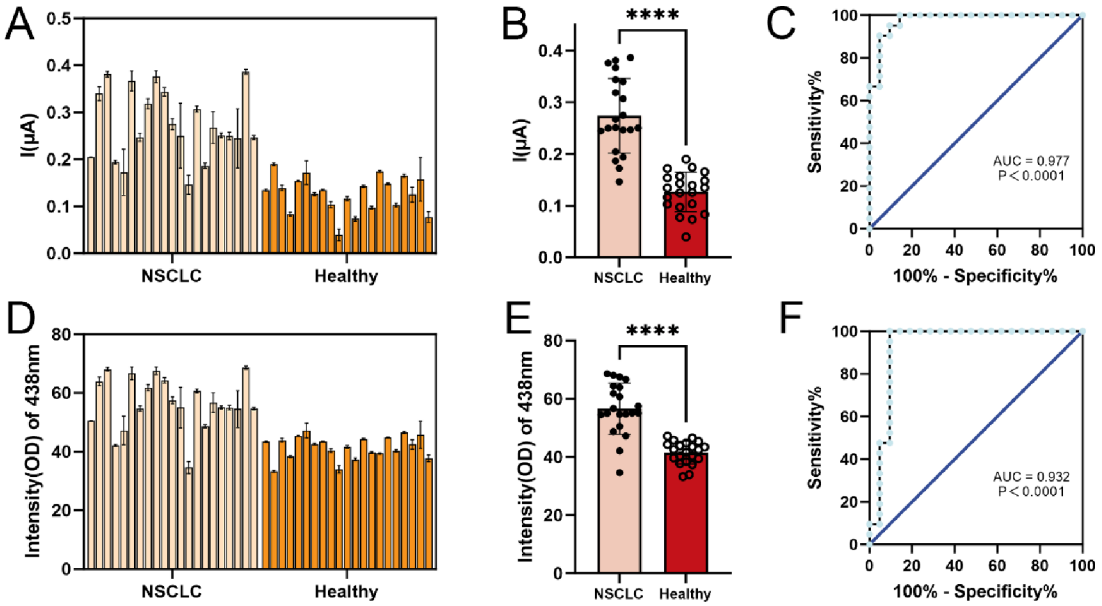

Figure 9. Constructed dual-modal aptasensor was used to detect CD63 protein on the surface of exosomes isolated from human serum samples, including NSCLC patients ($n = 21$) and healthy volunteers ($n = 21$) (Electrochemical analysis (A), Fluorescence analysis (D)). There is a significant difference in CD63 expression between cancer patients and healthy controls ($P < 0.0001$) (electrochemical analysis (B), fluorescence analysis (E)). (C) ROC curve confirming the ability of the dual-modal aptasensor to differentiate between cancer patients and normal controls (Electrochemical analysis (C), Fluorescence analysis (F)). Triplicate experiments were used to calculate error bars.

specifically binds to exosomes, forming the Exo/Apt2−Co@g-C_3N_4@PB complex. The gradual enhancement in fluorescence intensity is due to the strong fluorescence efficiency of Co@g-C_3N_4@PB.[46]

To evaluate this dual-modal aptasensor, we compare its performance in exosome detection with previous methods, as shown in Table.S1. In contrast, this dual-modal aptasensor combines the advantages of electrochemical and fluorescence analysis. In the sensing platform, due to the presence of PB,[47] it maintains high electrochemical/electrocatalytic performance even at low oxidation−reduction potentials, while avoiding interference with the electrochemical signal. Consequently, the electrochemical analysis method has a lower LOD and a wider linear range; whereas the fluorescence analysis method has a shorter detection time. It is worth noting that due to the metal-enhanced fluorescence effect of Co ions and Fe ions in the fluorescent label Co@g-C_3N_4@PB, the LOD of the fluorescence analysis method of this sensing platform is also exceptionally good. During actual detection processes, fluorescence inverted microscopy can be used to conduct a preliminary screening of large batches of samples, quickly identifying suspected positive samples. Subsequently, either electrochemical or fluorescence analysis methods can be used for more accurate quantification (Figure 8).

In the assessment of the performance of the dual-mode aptasensor, reproducibility plays a critical role. By utilizing 10 independently fabricated dual-mode aptasensors under identical conditions, we detect exosomes at a concentration of 10^4 particles/mL. The corresponding current peaks and fluorescence intensities at 438 nm are recorded for each aptasensor (Figure S6A,D). The relative standard deviation (RSD) for electrochemical analysis is 5.01%, and for fluorescence analysis, it is 5.06%, demonstrating the commendable reproducibility of the dual-mode aptasensor. To assess the stability of the developed dual-mode aptasensor, the current peak and fluorescence intensity at 438 nm are recorded every 5 days (Figure S6B,E). The findings reveal that even after 20 days of storage the current peak retains 89.27% of its initial value and the fluorescence intensity maintains 84.80% of the initial value. These results affirm the acceptable stability of the aptasensor. These results are attributed to the stability of Co@g-C_3N_4@PB, rendering the constructed dual-mode sensor reliable and stable.

Due to the complexity of clinical sample matrices, it is necessary to evaluate the specificity of the dual-mode aptasensor by measuring common interfering substances in serum before applying it to clinical serum sample detection (Figure S6C,F). Bovine serum albumin (BSA), immunoglobulin G (IgG), and glucose are assessed at concentrations of 4 mg/mL, serving as potential interfering substances. Additionally, exosomes at concentrations of 1×10^4 particles/mL are included in the study. Results indicate that the blank sample exhibits the lowest intensity, while the current peak value and fluorescence intensity value at 438 nm for A549 exosomes are significantly higher than those for the other three interfering substances. The results indicate that the bimodal adaptor sensor exhibits excellent performance, sensitively and selectively detecting exosomes in biological samples.

To assess the accuracy of the dual-mode aptasensor, varying concentrations of exosomes are introduced into serum samples (Table S2). The recoveries ranged from 97.07% to 108.4% for electrochemical analysis and from 92.9% to 108.0% for fluorescence analysis, respectively. The validation confirms the high feasibility and reliability of the dual-mode aptasensor for accurately detecting exosomes in real-life samples.

3.8. Clinical Sample Analysis. To validate the practical applicability of the developed dual-mode aptasensor, we obtained 42 clinical serum samples from Shanghai Pudong Hospital, comprising 21 healthy volunteers and 21 patients diagnosed with NSCLC. Exosome isolation is carried out using an exosome isolation kit. The constructed dual-mode aptasensor is employed for analysis, recording the peak current and fluorescence intensity at 438 nm.

https://doi.org/10.1021/acsomega.4c02346
ACS Omega 2024, 9, 34493−34506

Figure 9A,D illustrates the variations in peak current and fluorescence intensity at 438 nm. We observe significantly elevated peak current and fluorescence intensity at 438 nm in confirmed NSCLC patients compared to healthy volunteers.

As shown in Figure 9B,E, a significant disparity in CD63 expression between NSCLC patients and healthy volunteers is evident ($P < 0.0001$). The receiver operating characteristic curve (ROC) further validates the high accuracy of the dual-mode aptasensor in distinguishing CD63 protein expression levels on the exosome surface derived from serum of NSCLC patients and healthy volunteers. The area under the curve (AUC) is 0.977 for electrochemical analysis (Figure 9C) and 0.932 for fluorescence analysis (Figure 9F), respectively.

Compared to healthy volunteers, exosomes derived from the serum of NSCLC patients are more abundant.[48] Meanwhile, the expression level of the CD63 protein on the surface of exosomes from the serum of NSCLC patients is higher.[49] This aptasensor can distinguish between serum samples from healthy volunteers and those from NSCLC patients, which is advantageous for early cancer screening and the diagnosis of potential NSCLC patients with respiratory symptoms in clinical practice. Even more excitingly, the conventional electrochemical analysis process takes 18 h to screen out 21 NSCLC patients from 42 volunteers. However, employing a dual-modal aptasensor drastically reduces this time frame. Initially, all 42 samples undergo fluorescence qualitative analysis using a fluorescence inverted microscope, enabling the identification of suspected positive samples within just 1 h. The electrochemical analysis method exhibits a 4.5% higher detection efficiency than the fluorescence analysis method and has a wider linear range. Subsequently, suspected positive samples undergo more precise quantitative analysis using electrochemical methods. This significantly reduces both the cost and the time required for large sample screening in clinical practice.

4. CONCLUSIONS

In summary, we utilize aptamer-modified Co@g-C_3N_4@PB to successfully develop an electrochemical and fluorescent dual-mode aptasensor for the sensitive detection of NSCLC exosomes. Our dual-mode aptasensor outperforms other reported methods in terms of sensitivity for exosome detection. Importantly, our method is renowned for its simplicity and intuitiveness, integrating the advantages of electrochemical and fluorescence analysis methods. During the actual detection process, a fluorescence inverted microscope can be used for the preliminary screening of large batches of samples, facilitating the rapid identification of the suspected positive samples. Subsequently, more accurate quantification can be achieved using either electrochemical or fluorescence analysis methods. This approach enables swift qualitative screening and precise quantitative detection, thereby enhancing the efficiency of clinical analysis. With its potential for point-of-care testing, our method holds significant promise for future advancements in cancer diagnosis.

■ ASSOCIATED CONTENT

Supporting Information

The Supporting Information is available free of charge at https://pubs.acs.org/doi/10.1021/acsomega.4c02346.

Characterization of exosomes (Figure S1); z-potentials, TEM characterization, and distribution of metallic elements of g-C_3N_4 and metallic elements@g-C_3N_4 (Figure S2); fluorescence spectroscopy and fluorescence image of g-C_3N_4 and metallic elements@g-C_3N_4 (Figure S3); fluorescence spectroscopy of g-C_3N_4, Co@g-C_3N_4, Co, g-C_3N_4@PB, and Co@g-C_3N_4@PB (Figure S4); optimization of experimental conditions for dual-mode aptasensor (Figure S5); study on the reproducibility, stability, and specificity of dual-modal aptasensors (Figure S6); comparison of different methods for exosomes detection (Table S1); analysis of exosomes in serum using the dual-mode aptasensor (Table S2) (PDF)

■ AUTHOR INFORMATION

Corresponding Authors

Hongzhi Pan − *Collaborative Research Center, Shanghai University of Medicine and Health Sciences, Shanghai 201399, China*; orcid.org/0000-0003-4440-4616; Email: panhongzhi@163.com

Dong Chang − *Department of Clinical Laboratory, Shanghai Pudong Hospital, Fudan University Pudong Medical Center, Shanghai 201399, China*; Email: changdongydy@163.com

Authors

Xin Xu − *Department of Clinical Laboratory, Shanghai Pudong Hospital, Fudan University Pudong Medical Center, Shanghai 201399, China*; orcid.org/0009-0003-3992-6636

Ze Zhang − *Department of Clinical Laboratory, Shanghai Pudong Hospital, Fudan University Pudong Medical Center, Shanghai 201399, China*

Hongwei Yu − *Department of Clinical Laboratory, Shanghai Pudong Hospital, Fudan University Pudong Medical Center, Shanghai 201399, China*

Tong Shen − *Department of Clinical Laboratory, Shanghai Pudong Hospital, Fudan University Pudong Medical Center, Shanghai 201399, China; Hebei Medical University, Shijiazhuang, Hebei 050011, China*

Complete contact information is available at: https://pubs.acs.org/10.1021/acsomega.4c02346

Notes

The authors declare no competing financial interest.

This study has been approved by the Ethics Committee of Pudong Hospital Affiliated to Fudan University, approval number: 2020-M-11

■ ACKNOWLEDGMENTS

This research was supported by the National Natural Science Foundation of China (Grant No. 82073600, 82204098), the Project of Key Medical Specialty and Treatment Center of Pudong Hospital of Fudan University (Grant No. Zdzk2020-23), the Key Discipline Construction Project of Pudong Health and Family Planning Commission of Shanghai (Grant No. PWZxk2022-08), Shanghai Pudong Hospital Institute level Introduction of Talents Scientific Research Launching Grant Program (Grant No. YJYJRC202115), and Fudan Zhangjiang Clinical Innovation Fund Project (Grant No. KP0202122). The Research Ethics Committee of Shanghai Pudong Hospital (Shanghai, China) granted ethical approval.

■ REFERENCES

(1) Xu, M. Y.; Hao, Y.; Zeng, X. H.; Si, J. F.; Song, Z. B. Immune checkpoint inhibitors beyond first-line progression with prior immunotherapy in patients with advanced non-small cell lung cancer. *J. Thorac. Dis.* **2023**, *15* (4), 1648−1657.

(2) Henschke, C.; Huber, R.; Jiang, L.; Yang, D.; Cavic, M.; Schmidt, H.; Kazerooni, E.; Zulueta, J. J.; Dos Santos, R. S.; Ventura, L.; members of the Diagnostics Working Group, Early Detection and Screening, Committee. Perspective on Management of Low-Dose Computed Tomography Findings on Low-Dose Computed Tomography Examinations for Lung Cancer Screening. From the International Association for the Study of Lung Cancer Early Detection and Screening Committee. *J. Thorac. Oncol.* **2024**, *19* (4), 565−580.
(3) Hendrick, R. E.; Smith, R. A. Benefit-to-radiation-risk of low-dose computed tomography lung cancer screening. *Cancer* **2024**, *130* (2), 216−223.
(4) Mu, R. H.; Meng, Z. N.; Zhang, X. D.; Guo, Z. X.; Zheng, W.; Zhuang, Z. Y.; Zhu, X. Q. Parameters of Dual-layer Spectral Detector CT Could be Used to Differentiate Non-Small Cell Lung Cancer from Small Cell Lung Cancer. *Curr. Med. Imaging* **2022**, *18* (10), 1070−1078.
(5) Faiman, B.; Kurtin, S. E.; Persinger, R. Biomarker Pursuit: Keeping Current With Novel Biomarkers in Hematology/Oncology. *J. Adv. Pract. Oncol.* **2023**, *14* (3), 223−226.
(6) Aung, T. N.; Bates, K. M.; Rimm, D. L. High-Plex Assessment of Biomarkers in Tumors. *Mod. Pathol.* **2024**, *37* (3), No. 100425.
(7) Gan, T.; An, W.; Long, Y.; Wang, J.; Zhang, H.; Liao, M. Correlation between carcinoembryonic antigen (CEA) expression and EGFR mutations in non-small-cell lung cancer: a meta-analysis. *Clin. Transl. Oncol.* **2023**, *10*, 991 DOI: 10.1007/s12094-023-03339-7.
(8) Chen, F.; Zhang, X. Predictive value of serum SCCA and CYFRA21−1 levels on radiotherapy efficacy and prognosis in patients with non-small cell lung cancer. *Biotechnol. Genet. Eng. Rev.* **2023**, *10*, 1 DOI: 10.1080/02648725.2023.2208449.
(9) Wu, L. H.; Chen, L.; Wang, Q. Y.; Wang, Y. T. Correlation between HRCT signs and levels of CA125, SCCA, and NSE for different pathological types of lung cancer. *Eur. Rev. Med. Pharmacol. Sci.* **2023**, *27* (9), 4162−4168.
(10) Malapelle, U.; Pisapia, P.; Addeo, A.; Arrieta, O.; Bellosillo, B.; Cardona, A. F.; Cristofanilli, M.; De Miguel-Perez, D.; Denninghoff, V. C.; Durán, I.; Jantus-Lewintre, E.; Nuzzo, P. V.; O'Byrne, K.; Pauwels, P.; Pickering, E. M.; Raez, L. E.; Russo, A.; Serrano, M. J.; Gandara, D. R.; Troncone, G.; Rolfo, C. Liquid biopsy from research to clinical practice: focus on non-small cell lung cancer. *Expert Rev. Mol. Diagn.* **2021**, *21* (11), 1165−1178.
(11) Wu, Z.; Yang, Z.; Dai, Y.; Zhu, Q.; Chen, L. A. Update on liquid biopsy in clinical management of non-small cell lung cancer. *OncoTargets Ther.* **2019**, *12* (4), 5097−5109.
(12) Chang, W.; Zhu, J.; Yang, D.; Shang, A.; Sun, Z.; Quan, W.; Li, D. Plasma versican and plasma exosomal versican as potential diagnostic markers for non-small cell lung cancer. *Respir. Res.* **2023**, *24* (1), 13.
(13) Yang, P.; Zhang, Y.; Zhang, R.; Wang, Y.; Zhu, S.; Peng, X.; Zeng, Y.; Yang, B.; Pan, M.; Gong, J.; Ba, H. Plasma-derived exosomal immunoglobulins IGHV4−4 and IGLV1−40 as new non-small cell lung cancer biomarkers. *Am. J. Cancer Res.* **2023**, *13* (5), 1923−1927.
(14) Li, M. X.; Liu, T.; Cheng, W.; Jin, H.; Wang, X. W. A test of miR-128−3p and miR-33a-5p in serum exosome as biomarkers for auxiliary diagnosis of non-small cell lung cancer. *J. Thorac. Dis.* **2023**, *15* (5), 2616−2626.
(15) Baran, K.; Waśko, J.; Kryczka, J.; Boncela, J.; Jabłoński, S.; Kolesińska, B.; Brzeziańska-Lasota, E.; Kordiak, J. The Comparison of Serum Exosome Protein Profile in Diagnosis of NSCLC Patients. *Int. J. Mol. Sci.* **2023**, *24* (18), 13669.
(16) Auger, C.; Brunel, A.; Darbas, T.; Akil, H.; Perraud, A.; Bégaud, G.; Bessette, B.; Christou, N.; Verdier, M. Extracellular Vesicle Measurements with Nanoparticle Tracking Analysis: A Different Appreciation of Up and Down Secretion. *Int. J. Mol. Sci.* **2022**, *23* (4), 2310.
(17) Wen, J.; Zhang, Z. J.; Feng, G.; Zhang, Y.; Li, H. Z.; Lambert, C.; Mallouk, N.; Li, G. R. Transmission electron microscopy assessment of a novel method for isolating pure exosomes from serum. *Biotechnol. Histochem.* **2023**, *98* (6), 391−395.
(18) Zhou, X.; Tang, W.; Zhang, Y.; Deng, A.; Guo, Y.; Qian, L. Liposome-exosome hybrids for < i > in situ</i> detection of exosomal miR-1246 in breast cancer. *Analyst* **2024**, *149* (2), 403−409.
(19) Gonzalez, A. G. A.; Ortiz-Lazareno, P. C.; Solorzano-Ibarra, F.; Gutierrez-Franco, J.; Tellez-Bañuelos, M. C.; Bueno-Topete, M. R.; del Toro-Arreola, S.; Haramati, J. A Modified Method for the Quantification of Immune Checkpoint Ligands on Exosomes from Human Serum using Flow Cytometry. *Technol. Cancer Res. Treat.* **2023**, *22*, 153303382211503.
(20) Fan, Z.; Zhou, J.; Shu, Q.; Dong, Y.; Li, Y.; Zhang, T.; Bai, G.; Yu, H.; Lu, F.; Li, J.; Zhao, X. Aptamer-bivalent-cholesterol-mediated proximity entropy-driven exosomal protein reporter for tumor diagnosis. *Biosens. Bioelectron.* **2024**, *251*, No. 116104.
(21) An, J.; Park, H.; Kim, J.; Park, H.; Kim, T. H.; Park, C.; Kim, J.; Lee, M. H.; Lee, T. K. Extended-Gate Field-Effect Transistor Consisted of a CD9 Aptamer and MXene for Exosome Detection in Human Serum. *ACS Sens.* **2023**, *8*, 3174 DOI: 10.1021/acssensors.3c00879.
(22) Sequeira-Antunes, B.; Ferreira, H. A. Nucleic Acid Aptamer-Based Biosensors: A Review. *Biomedicines* **2023**, *11* (12), 3201.
(23) Sun, Y. J.; Jin, H.; Jiang, X. W.; Gui, R. J. Assembly of Black Phosphorus Nanosheets and MOF to Form Functional Hybrid Thin-Film for Precise Protein Capture, Dual-Signal and Intrinsic Self-Calibration Sensing of Specific Cancer-Derived Exosomes. *Anal. Chem.* **2020**, *92* (3), 2866−2875.
(24) Singh, S.; Pathak, A.; Kumar, S.; Malik, P. S.; Elangovan, R. Rapid immunomagnetic co-capture assay for quantification of lung cancer associated exosomes. *J. Immunol. Methods* **2022**, *508*, No. 113324.
(25) Zhang, W.; Tian, Z.; Yang, S.; Rich, J.; Zhao, S.; Klingeborn, M.; Huang, P. H.; Li, Z.; Stout, A.; Murphy, Q.; Patz, E.; Zhang, S.; Liu, G.; Huang, T. J. Electrochemical micro-aptasensors for exosome detection based on hybridization chain reaction amplification. *Microsyst. Nanoeng.* **2021**, *7* (1), 8.
(26) Yi, P.; Luo, D.; Gao, Z.; Chen, Q. H.; Zhou, Y. J. Fluorescent aptasensor based on the MNPs-CRISPR/Cas12a-TdT for the determination of nasopharyngeal carcinoma-derived exosomes. *Microchim. Acta* **2023**, *190* (2), 9.
(27) Yan, X.; Zhang, M.; Chen, Y.; Wu, Y.; Wu, R.; Wan, Q.; Liu, C.; Zheng, T.; Feng, R.; Zhang, J.; Chen, C.; Xia, C.; Zhu, Q.; Sun, X.; Qian, Q.; Han, B. Synergy of Cu/C3N4 Interface and Cu Nanoparticles Dual Catalytic Regions in Electrolysis of CO to Acetic Acid. *Angew. Chem.-Int. Ed.* **2023**, *62* (22), 9.
(28) Jiang, B.; Guo, Z. J.; Liang, M. M. Recent progress in single -atom nanozymes research. *Nano Res.* **2023**, *16* (2), 1878−1889.
(29) Kjeldgaard, S.; Dugulan, I.; Mamakhel, A.; Wagemaker, M.; Iversen, B. B.; Bentien, A. Strategies for synthesis of Prussian blue analogues. *R. Soc. Open Sci.* **2021**, *8* (1), 201779.
(30) Li, W.; Li, W.; Guo, Z.; Song, Y.; Tang, S.; Ma, Y.; Xing, X.; Wang, Q. Synthesis of Atomically Thin g-C(3)N(4) Nanosheets via Supercritical CO(2) Doping with Single-Atom Cobalt for Photocatalytic Hydrogen Evolution. *ACS Appl. Mater. Interfaces* **2021**, *13* (44), 52560−52570.
(31) Perebeinos, V.; Tersoff, J.; Avouris, P. Radiative lifetime of excitons in carbon nanotubes. *Nano Lett.* **2005**, *5* (12), 2495−9.
(32) Wang, Z.; Zheng, L.; Cheng, Q.; Li, X.; Huang, L.; Lu, Y. Metal-enhanced fluorescence of graphene oxide sheets. *Anal Bioanal Chem.* **2022**, *414* (12), 3625−3630.
(33) Hong, G. S.; Tabakman, S. M.; Welsher, K.; Wang, H. L.; Wang, X. R.; Dai, H. J. Metal-Enhanced Fluorescence of Carbon Nanotubes. *J. Am. Chem. Soc.* **2010**, *132* (45), 15920−15923.
(34) Yu, J. M.; Yang, L. R.; Liang, X. F.; Dong, T. T.; Liu, H. Z. Bare magnetic nanoparticles as fluorescence quenchers for detection of thrombin. *Analyst* **2015**, *140* (12), 4114−4120.
(35) Wang, Z.; Zhang, Z.; Pan, H.; Chang, D. An ultrasensitive aptasensor for exosomes detection based on biotin-streptavidin and MXenes. *Anal. Biochem.* **2023**, *676*, No. 115233.
(36) Zhang, H.; Wang, Z.; Wang, F.; Zhang, Y.; Wang, H.; Liu, Y. Ti(3)C(2) MXene mediated Prussian blue in situ hybridization and electrochemical signal amplification for the detection of exosomes. *Talanta* **2021**, *224* (10), No. 121879.

https://doi.org/10.1021/acsomega.4c02346
ACS Omega 2024, 9, 34493−34506

(37) Jang, M.; Choi, G.; Choi, Y. Y.; Lee, J. E.; Jung, J. H.; Oh, S. W.; Han, D. H.; Lee, H.; Park, J. H.; Cheong, J. H.; Kim, P. Extracellular vesicle (EV)-polyphenol nanoaggregates for microRNA-based cancer diagnosis. *NPG Asia Mater.* **2019**, *11*, 10.
(38) Xu, S.; Hartvickson, S.; Zhao, J. X. Increasing surface area of silica nanoparticles with a rough surface. *ACS Appl. Mater. Interfaces* **2011**, *3* (6), 1865−72.
(39) Koh, H.; An, H.; Jung, J.; Song, D. The prognostic significance of CD63 expressionin patients with non-small cell lung cancer. *Pol J. Pathol* **2019**, *70* (3), 183−188.
(40) Folkmanis, K.; Junk, E.; Merdane, E.; Folkmane, I.; Folkmanis, V.; Ivanovs, I.; Eglitis, J.; Jakubovskis, M.; Laabs, S.; Isajevs, S.; Lietuvietis, V. Clinicopathological Significance of Exosomal Proteins CD9 and CD63 and DNA Mismatch Repair Proteins in Prostate Adenocarcinoma and Benign Hyperplasia. *Diagnostics (Basel)* **2022**, *12* (2), 287.
(41) Mathieu, M.; Névo, N.; Jouve, M.; Valenzuela, J. I.; Maurin, M.; Verweij, F. J.; Palmulli, R.; Lankar, D.; Dingli, F.; Loew, D.; Rubinstein, E.; Boncompain, G.; Perez, F.; Théry, C. Specificities of exosome versus small ectosome secretion revealed by live intracellular tracking of CD63 and CD9. *Nat. Commun.* **2021**, *12* (1), 4389.
(42) Qiu, G.; Thakur, A.; Xu, C.; Ng, S. P.; Wu, C. M. L. Detection of Glioma-derived Exosomes with the Biotinylated Antibody-Functionalized Titanium Nitride Plasmonic Biosensor. *Adv. Funct. Mater.* **2018**, *29* (9), 1806761.
(43) Sun, Y.; Jin, H.; Jiang, X.; Gui, R. Assembly of Black Phosphorus Nanosheets and MOF to Form Functional Hybrid Thin-Film for Precise Protein Capture, Dual-Signal and Intrinsic Self-Calibration Sensing of Specific Cancer-Derived Exosomes. *Anal. Chem.* **2020**, *92* (3), 2866−2875.
(44) Wang, P.; Yuan, X. X.; Cui, Z.; Xu, C. Y.; Sun, Z. L.; Li, J. H.; Liu, J. S.; Tian, Y.; Li, H. D. A Nanometer-Sized Graphite/Boron-Doped Diamond Electrochemical Sensor for Sensitive Detection of Acetaminophen. *ACS Omega* **2021**, *6* (9), 6326−6334.
(45) Massah, R. T.; Jiokeng, S. L. Z.; Liang, J.; Njanja, E.; Ntep, T. M. M.; Spiess, A.; Rademacher, L.; Janiak, C.; Tonle, I. K. Sensitive Electrochemical Sensor Based On an Aminated MIL-101(Cr) MOF for the Detection of Tartrazine. *ACS Omega* **2022**, *7* (23), 19420−19427.
(46) Qu, B.; Sun, J.; Li, P.; Jing, L. Current advances on g-C3N4-based fluorescence detection for environmental contaminants. *J. Hazard. Mater.* **2022**, *425*, No. 127990.
(47) Wang, G.; Liu, J.; Dong, H.; Geng, L.; Sun, J.; Liu, J.; Dong, J.; Guo, Y.; Sun, X. A dual-mode biosensor featuring single-atom Fe nanozyme for multi-pesticide detection in vegetables. *Food Chem.* **2024**, *437*, No. 137882.
(48) Rabinowits, G.; Gerçel-Taylor, C.; Day, J. M.; Taylor, D. D.; Kloecker, G. H. Exosomal microRNA: a diagnostic marker for lung cancer. *Clinical lung cancer* **2009**, *10* (1), 42−6.
(49) Sandfeld-Paulsen, B.; Jakobsen, K. R.; Bæk, R.; Folkersen, B. H.; Rasmussen, T. R.; Meldgaard, P.; Varming, K.; Jørgensen, M. M.; Sorensen, B. S. Exosomal Proteins as Diagnostic Biomarkers in Lung Cancer. *J. Thorac. Oncol.* **2016**, *11* (10), 1701−1710.

https://doi.org/10.1021/acsomega.4c02346
ACS Omega 2024, 9, 34493−34506